Antisymmetric Localization by a Defect in an Acoustic Band-Gap Structure

Zhi-Yong Tao,[1,2,*] Ting Liu,[1] Huan Liu,[1] and Ya-Xian Fan[2]

[1]*Key Laboratory of In-fiber Integrated Optics, Ministry Education of China, Harbin Engineering University, Harbin 150001, People's Republic of China*

[2]*Academy of Marine Information Technology, Guilin University of Electronic Technology, Beihai 536000, People's Republic of China*

The introduction of defects into photonic and phononic crystals leads to defect states arising within the former forbidden bands and has been found in applications for making functional devices. These defect states, due to Bragg resonances, commonly have an antinode of energy localization in the center of the defect. We report our experimental observation and theoretical and numerical validation of a dipole-like antisymmetric localization of acoustic waves in a defect-embedded periodic duct. Our measurements and analysis reveal that the antisymmetric localization that we observe arises from an extraordinary transmission by non-Bragg resonances. Our study can inspire the exploration of similar defect states in other wave systems and broaden the applications for making functional devices, such as acoustical and optical tweezers, spatial sound and/or light modulators, and signal and/or structure detectors.

I. INTRODUCTION

Since the pioneering work by Lord Rayleigh in the 1880s on waves in periodic structures [1], a number of researchers have devoted themselves to theories of electric behavior in periodic lattices (natural crystals); around the 1920s, Bloch built the basis of solid-state electronics and energy-band theories [2,3]. Photonic and phononic crystals [4–7] in which the band gap is usually attributed to Bragg resonances [8–10] have been investigated extensively. In periodic-waveguide structures, however, there is another type of resonance that is less studied, termed the "non-Bragg resonance" [11,12]. Non-Bragg resonances are caused by resonances of different transverse modes that also result in forbidden bands. Non-Bragg resonances have been proved to be more intense than Bragg types in waveguides because of the existence of unavoidable higher-order transverse modes, as successively observed in acoustics [13], water-surface waves [14], terahertz waves [15], and microwaves [16].

When a defect such as a point imperfection or a dislocation in a crystal is introduced into a periodic structure, the physical and chemical properties of the materials are essentially modulated [17,18]. The introduction of defects into photonic and phononic crystals leads to defect states arising within the former forbidden bands and has found application for making functional devices [19–21]. These defect states due to Bragg resonances commonly have an antinode of energy localization in the center of the defect [22–24]. The defect states have also been experimentally observed in a waveguide structure for optical [25] and acoustical [26] waves. However, the defect states associated with non-Bragg resonances are still an open question: Can the defect lead to energy localization when the non-Bragg resonance occurs? If so, do the defect states in non-Bragg resonances have the same characteristics as the previously observed localization in Bragg resonances?

In this paper, we report our observation of a defect state that has an antisymmetric localization with a stationary point in the middle of the defect and arises from non-Bragg resonances. This non-Bragg defect state is in contrast to the traditional localization. In our waveguide, the localization of the defect produces not only an antinode but also a dipole distribution with a node in the center. We find that the traditional antinode arises in the Bragg gap while the unexpected dipole appears in the non-Bragg gap. Further measurements and modeling confirm the contributions of the high-order mode interactions on the unusual localization.

II. LOCALIZATION WITH A NODE

A schematic of the assembled waveguide and the experimental setup is illustrated in the top portion of Fig. 1. The speaker is used to excite the sound from the left end of the waveguide, while the microphone is inserted from the other open end to detect the transmitted signals. The imperfect structure is made by tightening the thread of two periodic ducts to a defect. The proposed imperfect
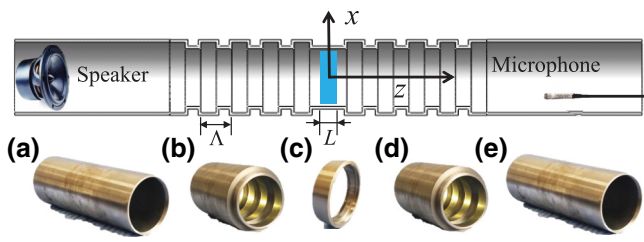
_____
*zytao@hrbeu.edu.cn

FIG. 1.   The experimental setup and corrugated waveguide with a defect (blue) at the center. The top portion shows the schematic diagram of the assembled waveguide for detection. The shaded area denotes the inserted defect. The bottom portion (a)–(e) consists of photographs of the five sections of the waveguide made of steel pipe. The speaker and microphone are placed inside the waveguide. The corrugation period is Λ and the defect length is L.

duct consists of five steel pipes, as shown in the bottom portion of Fig. 1. The two 500-mm-long straight ducts shown in Figs. 1(a) and 1(e), each with an inner diameter of 132 mm, are placed at the inlet and outlet of the imperfect duct to reform the incident and output acoustic waves, respectively. The perfect duct is divided into two parts to make it more convenient to manufacture. Each part is constructed by periodically lathing the inner diameter of a thick wall steel pipe, as shown in Figs. 1(b) and 1(d). The wide and narrow inner diameters are 132 and 108 mm, respectively. The periodicity is $\Lambda = 60$ mm. Another straight duct with an inner diameter of 108 mm and a net length of 22 mm is also lathed [Fig. 1(c)] as the inserted defect to the perfect duct. In order to complete the process of manufacturing the imperfect duct, we tighten the thread processed at the two ends of each duct. In the lathing process, we select steel pipes of sufficient size to guarantee a wall thickness greater than 4 mm in the whole elaborated duct, which means that the wall will not vibrate in the experiments and can theoretically be treated as a rigid boundary.

In the experiments (for the details of the measurements, see the Appendix), we move the microphone in the inlet and outlet straight ducts along the z axis to detect the maximum sound pressures P_{in} and P_{out}, and then we calculate the transmission coefficient using

$$T = 20 \log_{10} \left\| \frac{P_{\mathrm{out}}}{P_{\mathrm{in}}} \right\|, \qquad (1)$$

where T is the transmission coefficient, depicted by the red solid line in Fig. 2. With the finite-element method (FEM) in the Comsol multiphysics software, we perform simulations of the acoustic pressure fields using an axisymmetric model (for details of the simulations, see the Appendix). Without the defect, the calculated transmission of a perfectly periodic waveguide (the dashed line in Fig. 2) illustrates the Bragg (gray shading) and non-Bragg gaps (cyan

shading). In the waveguide, the non-Bragg gap appears in the higher-frequency range relative to the Bragg one and the sound attenuation is much more intense [13]. Both the experimental (solid red line) and numerical (solid black line) results show that the two extraordinary transmitted peaks arises in the non-Bragg gap, but only one extraordinary peak with a wider bandwidth appears in the Bragg gap. The frequency deviations between the measured and simulated data are ascribed to slight machining errors from the designed structure. Although the oscillations and tiny additional peaks in the non-Bragg gap are caused by the background noise around -60 dB and slight machining imperfections, respectively, we still observe defect states arising in the non-Bragg gap. The measurements not only confirm that defect states can be achieved in non-Bragg gap as well, but also indicate their complex mechanism and the difficulty in detection due to the extreme narrowness of the two peaks.

To clarify the characteristics of the non-Bragg defect states, we also measure the sound pressure along the symmetry axis of the cylindrical duct. Because the second peak is very close to the right-hand edge, we focus on the first peak at 3866 Hz in the non-Bragg gap, as well as the peak at 2796 Hz in the Bragg gap. The microphone is moved along the z axis by 400 mm, which places it in the middle of the defect section. We then record the sound pressure in 5 mm steps. The sound pressures at 2796 and 3866 Hz are shown in Figs. 3(a) and 3(b), respectively, by the circles connected by the dashed lines. The extraordinary discovery is the stationary point that appears in the middle of the defect at 3866 Hz in Fig. 3(b). As a reference, the expected antinode at 2796 Hz is exhibited in Fig. 3(a) for the defect state in the traditional Bragg gap. The simulated pressure distributions depicted by the black solid lines provide confidence in the observation of this alternative type of defect state. The extremely small sound pressure in the defect provides the experimental evidence of achieving acoustic localization with a central node.

In general, the energy localization in defects must lead to an antinode in the center, like the Bragg defect state that we obtain. The unexpected defect state with a node must have something to do with the different transverse modes involved in non-Bragg resonances. The transverse mode denotes the standing-wave pattern along the radial direction, which is the transverse eigenfunction of the waveguide system. In the cylindrical duct, it is the Bessel function $J_0(k_r r)$ with different radial wavenumber k_r. Beyond the Bragg resonances caused by the same transverse mode (the same k_r), non-Bragg ones are identified as interactions between different transverse modes (the different k_r). To reveal the effect of the high-order mode on the generation of the extraordinary defect state, we also measure the transverse distributions of the defect states and analyze their transverse-mode components. For the non-Bragg defect state (3866 Hz), we move the microphone
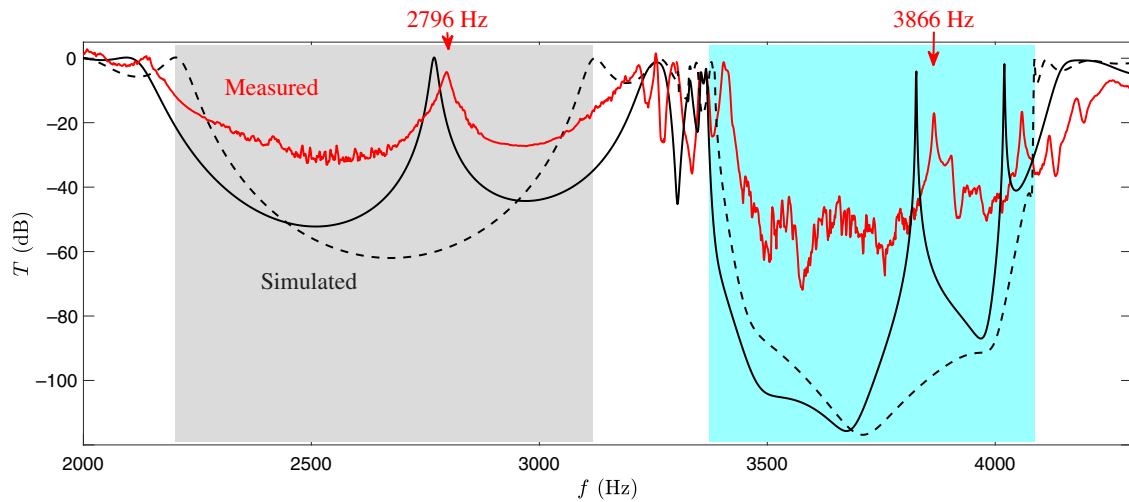
FIG. 2. The measured and simulated transmission spectra: the red solid line represents the measured defect states in the Bragg (2796 Hz) and non-Bragg (3866 Hz) gaps and the black solid line shows the simulated results. The frequency deviations are ascribed to slight machining imperfections. As a reference, the dashed line denotes the spectrum of the periodic waveguide without the defect and the gray- and cyan-shaded regions exhibit the Bragg and non-Bragg gaps, respectively.

along the z axis to the location at which the sound pressure maximum occurs ($z = -27$ mm). We obtain two maxima along the z axis in the non-Bragg defect states and the transverse distributions are similar, so only the first maximum is presented here. With the longitudinal position fixed, the microphone is moved along the x axis in 1 mm steps, from -50 to 50 mm. The sound pressure

self-normalized at 3866 Hz is depicted in Fig. 3(d) by the circles, while that of the Bragg defect at 2796 Hz is shown in Fig. 3(c), with the longitudinal maximum appearing at $z = -5$ mm. Also, the simulated transverse distributions (black solid lines) show the consistency between the numerical and measured results. To identify the transverse modes, we also perform a least-squares fit to the measured
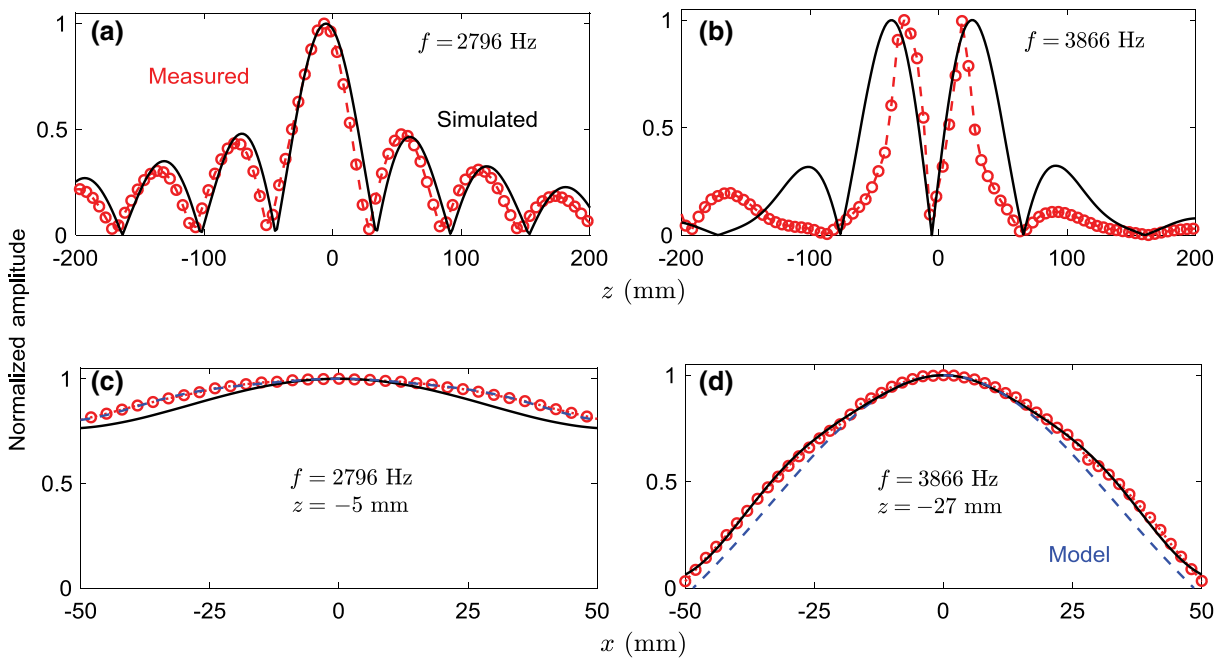

FIG. 3. The measured and simulated amplitudes of the sound pressures: the longitudinal sound pressures for (a) Bragg and (b) non-Bragg defect states exhibit the antinode and node in the defect, respectively, and the radial distributions at the longitudinal maxima of the (c) Bragg and (d) non-Bragg defect states indicate the involvement of the high-order transverse mode in creating the extraordinary acoustic localization. Each data set is normalized by its own maximum.

data by using a truncated model:

$$P(r) = a_0 J_0(k_{r,0} r/R) + a_1 J_0(k_{r,1} r/R), \qquad (2)$$

where $J_0(\cdot)$ is the zeroth-order Bessel function, $k_{r,0} = 0$ and $k_{r,1} = 3.8317$ denote the first two transverse modes, and the radius R is fixed at 54 mm, which is the radius of the defect. Only the first two transverse modes are considered here because the cutoff frequencies of the higher modes are far away from the range of interest. The superposition of the first two transverse modes is depicted in Figs. 3(c) and 3(d) by the blue dashed lines, indicating that most of the sound energy is concentrated in these two modes. With the total sound power $a_0 + a_1 = 100\%$, the ratios of the first and second transverse modes in the non-Bragg case are about 73.0% and 27.0%, respectively, whereas the ratios are 99.5% and 0.5% for the Bragg defect state. It is clear that the first and second transverse modes interact with each other in the non-Bragg defect state, whereas the traditional Bragg defect state can be hardly affected by the second transverse mode, exhibiting the quite different mechanism observed. It is because of this mode superposition that the extraordinary localization with the central node and the antisymmetric character are observed.

III. THE ANTISYMMETRY PROFILE

Based on non-Bragg resonances and non-Bragg defect states, we have created a localized acoustic field with a stationary point in the center of the defect. Near the node in the center, the sound pressure may have opposite phase and thus behave like a dipole, which is quite different from the previously observed defect states with a central antinode. Although the measured phase differences of the sound pressures on either side of the node can confirm the negative parity, the proposed antisymmetry can be represented more intuitively by the FEM results. The dipolar defect state is demonstrated by the simulated three-dimensional (3D) sound field and its projection, shown in Fig. 4(a). Both the central extraordinary node and the localized nature of the pressure field are apparent. Thus a strongly localized acoustic dipole exists in the center of the waveguide, which is induced by the mechanism provided by the non-Bragg resonances.

Beyond the non-Bragg resonances responsible for the antisymmetry, the localization characteristics can be explored using the FEM. The maximum sound pressure of the antisymmetric localization when the defect length increases from 0.1Λ to 0.8Λ is depicted by the circles in Fig. 4(b). It can be seen that the maximum amplitude appears at $L = 0.4\Lambda$, indicating the conditions for the most intense localization effect. This suggests that there is something special about the 0.4Λ defect, which is very close to the 0.37Λ size of the corrugated waveguide. To understand
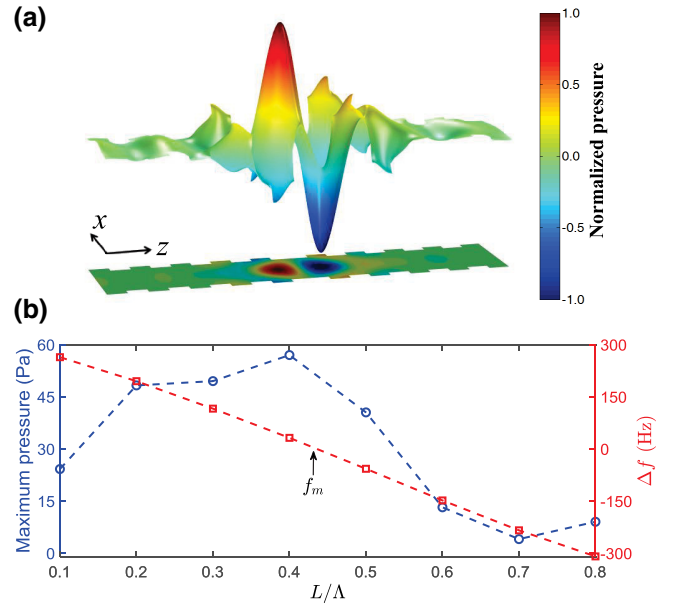

FIG. 4. (a) The numerical simulation of the 3D localized sound field exhibiting antisymmetry. (b) The maximum amplitude and frequency shifting of the antisymmetric localization versus the ratio of the defect width L and periodicity Λ.

the underlying causes, we calculate the peak frequency shifting of the antisymmetric localization from the center frequency of the non-Bragg gap at $f_m = 3766$ Hz. The frequency shift is proportional to the defect length. However, the most intense response occurs at only a small shift from the center frequency. Thus, a defect length of about 0.4Λ proves to be optimal for achieving the antisymmetric localization. Thus our choice of defect length is fortunate in that we are able to observe the antisymmetric feature with only a slight frequency deviation despite the machining inaccuracy.

IV. CONCLUSION

In conclusion, we produce an antisymmetric acoustic localization in the non-Bragg gap by inserting a straight duct as a defect in a perfectly periodic waveguide. This unusual type of defect state has a node in the center of the defect, beyond the normal antinode. The dipole signature is verified through measurements of the sound field along the symmetry axis of the duct and the results are supported by the FEM-based numerical simulations. The acoustic dipole is formed by the intense resonances of different transverse modes in the periodic waveguides. The first two transverse modes involved in the non-Bragg resonances are the major contributors to the creation of antisymmetric acoustic localizations, which can find application in microparticle manipulations [27–29]. The microparticles in a standing-wave field always experience a radiation force, depending on their locations between the pressure

nodes and antinodes, which can separate, concentrate, collect, and transport particles in applications such as bioengineering, materials and chemical engineering, and the pharmaceutical industry. Because of the ubiquity of wave phenomena, we believe that analogous antisymmetric localizations induced by non-Bragg resonance could also be observed in a wide range of modalities, including ultrasonics, optics, microwaves, and terahertz waves, which can definitely improve various functional devices, such as noncontact tweezers, spatial wave modulators, and signal and/or structure detectors.

ACKNOWLEDGMENTS

APPENDIX MEASUREMENTS AND SIMULATIONS

In the experiments, we generate a monochromatic signal using a National Instruments PCI-4461 card fitted inside a computer. The signal is routed through an amplifier to a coaxial monitor speaker, which radiates monochromic sound into the 500-mm-long straight duct. This straight duct channels the incident sound into the fundamental mode before propagating into the imperfect duct, which guarantees the simplicity of the waves entering the structure. At the other end of the structure, another straight duct is connected to reform the output impedance. To detect the sound pressures in the waveguide, we house a microphone (G.R.A.S. 46BE 1/4 in free-field microphone) in a 2-m-long steel pipe, retained by a 3D motorized translation stage. The received signals are sent back to the PCI-4461 card and then sampled at 200 kHz and stored in the computer. A tone-extraction analysis is performed to read out the frequency and amplitude of the signal. Thus, we can obtain the sound pressures throughout the imperfect duct.

In the simulations, only the periodic structure and the defect are considered, because the plane-wave radiation boundary conditions can be assigned to the inlet and outlet boundaries of the waveguide. For the other outer boundaries, hard-boundary sound conditions are selected. The acoustic properties in the duct are set at a density of 1.25 kg/m^3 and a sound speed (in air) of 343 m/s. The frequency of the incident plane wave is varied from 2000 to 4300 Hz with a step size of 1 Hz. Using the boundary integration tool, we calculate the incident and transmitted sound powers and the transmissions.

[1] L. Rayleigh, On the maintenance of vibrations by forces of double frequency, and on the propagation of waves through a medium endowed with a periodic structure, Philos. Mag. **24,** 145 (1887).

[2] L. Brillouin, *Wave Propagation in Periodic Structures* (Dover, New York, 1953).

[3] C. Elachi, Waves in active and passive periodic structures: A review, Proc. IEEE **64,** 1666 (1976).

[4] E. Yablonovitch, Inhibited Spontaneous Emission in Solid-State Physics and Electronics, Phys. Rev. Lett. **58,** 2059 (1987).

[5] S. John, Strong Localization of Photons in Certain Disordered Dielectric Superlattices, Phys. Rev. Lett. **58,** 2486 (1987).

[6] M. S.Kushwaha, P. Halevi, L. Dobrzynski, and B. Djafari-Rouhani, Acoustic Band Structure of Periodic Elastic Composites, Phys. Rev. Lett. **71,** 2022 (1993).

[7] F. R. Montero de Espinosa, E. Jiménez, and M. Torres, Ultrasonic Band Gap in a Periodic Two-Dimensional Composite, Phys. Rev. Lett. **80,** 1208 (1998).

[8] F. Cervera, L. Sanchis, J. V. Sánchez-Pérez, R. Martínez-Sala, C. Rubio, F. Meseguer, C. López, D. Caballero, and J. Sánchez-Dehesa, Refractive Acoustic Devices for Airborne Sound, Phys. Rev. Lett. **88,** 023902 (2001).

[9] T. Gorishnyy, C. K. Ullal, M. Maldovan, G. Fytas, and E. L. Thomas, Hypersonic Phononic Crystals, Phys. Rev. Lett. **94,** 115501 (2005).

[10] M. Farhat, S. Enoch, S. Guenneau, and A. B. Movchan, Broadband Cylindrical Acoustic Cloak for Linear Surface Waves in a Fluid, Phys. Rev. Lett. **101,** 134501 (2008).

[11] V. A. Pogrebnyak, Non-Bragg reflections in a periodic waveguide, Opt. Commun. **232,** 201 (2004).

[12] Z.-Y. Tao, Y.-M. Xiao, and X.-L. Wang, Non-Bragg resonance of standing acoustic wave in a cylindrical waveguide with sinusoidally perturbed walls, Chin. Phys. Lett. **22,** 394 (2005).

[13] Z. Tao, W. He, Y. Xiao, and X. Wang, Wide forbidden band induced by the interference of different transverse acoustic standing-wave modes, Appl. Phys. Lett. **92,** 121920 (2008).

[14] Y. Xiao, Z. Tao, W. He, and X. Wang, Non-Bragg resonance of surface water waves in a trough with periodic walls, Phys. Rev. E **78,** 016311 (2008).

[15] E. S. Lee, Y. B. Ji, and T.-I. Jeon, Terahertz band gap properties by using metal slits in tapered parallel-plate waveguides, Appl. Phys. Lett. **97,** 181112 (2010).

[16] V. A.Pogrebnyak and E. P. Furlani, Tunable Bloch Wave Resonances and Bloch Gaps in Uniform Materials with Reconfigurable Boundary Profiles, Phys. Rev. Lett. **116,** 206802 (2016).

[17] S. Wendt, P. T. Sprunger, E. Lira, G. K. H. Madsen, Z. Li, J. O. Hansen, J. Matthiesen, A. Blekinge-Rasmussen, E. Lægsgaard, B. Hammer, and F. Besenbacher, The role of interstitial sites in the Ti3*d* defect state in the band gap of titania, Science **320,** 1755 (2008).

[18] P. A. Schultz, Theory of Defect Levels and the "Band Gap Problem" in Silicon, Phys. Rev. Lett. **96,** 246401 (2006).

[19] O. Painter, R. K. Lee, A. Scherer, A. Yariv, J. D. O'Brien, P. D. Dapkus, and I. Kim, Two-dimensional photonic band-gap defect mode laser, Science **284,** 1819 (1999).

[20] J. C. Knight, J. Broeng, T. A. Birks, and P. St. J. Russell, Photonic band gap guidance in optical fibers, Science **282,** 1476 (1998).

[21] S. Noda, A. Chutinan, and M. Imada, Trapping and emission of photons by a single defect in a photonic bandgap structure, Nature **407,** 608 (2000).

[22] M. M. Sigalas, Elastic wave band gaps and defect states in two-dimensional composites, J. Acoust. Soc. Am. **101,** 1256 (1997).

[23] A. Khelif, A. Choujaa, B. Djafari-Rouhani, M. Wilm, S. Ballandras, and V. Laude, Trapping and guiding of acoustic waves by defect modes in a full-band-gap ultrasonic crystal, Phys. Rev. B **68,** 214301 (2003).

[24] M. L. Povinelli, S. G. Johnson, S. Fan, and J. D. Joannopoulos, Emulation of two-dimensional photonic crystal defect modes in a photonic crystal with a three-dimensional photonic band gap, Phys. Rev. B **64,** 075313 (2001).

[25] J. Ferrera, E. R. Thoen, G. Steinmeyer, S. Fan, J. D. Joannopoulos, L. C. Kimerling, H. I. Smith, J. S. Foresi, P. R. Villeneuveand, and E. P. Ippen, Photonic-bandgap microcavities in optical waveguides, Nature **390,** 143 (1997).

[26] J. N. Munday, C. BradBennett, and W. M.Robertson, Band gaps and defect modes in periodically structured waveguides, J. Acoust. Soc. Am. **112,** 1353 (2002).

[27] C. R. P. Courtney, C. E. M. Demore, H. Wu, A. Grinenko, P. D. Wilcox, S. Cochran, and B. W. Drinkwater, Independent trapping and manipulation of microparticles using dexterous acoustic tweezers, Appl. Phys. Lett. **104,** 154103 (2014).

[28] A. Franklin, A. Marzo, R. Malkin, and B. W. Drinkwater, Three-dimensional ultrasonic trapping of micro-particles in water with a simple and compact two-element transducer, Appl. Phys. Lett. **111,** 094101 (2017).

[29] A. Fornell, K. Cushing, J. Nilsson, and M. Tenje, Binary particle separation in droplet microfluidics using acoustophoresis, Appl. Phys. Lett. **112,** 063701 (2018).